9-27-2022

# Design of an Innovative Hybrid Sandwich Protective Device for Offshore Structures

Hozhabr Mozafari

Fabio Distefano

Gabriella Epasto

Linxia Gu

Emanoil Linul

*See next page for additional authors*

Authors
Hozhabr Mozafari, Fabio Distefano, Gabriella Epasto, Linxia Gu, Emanoil Linul, and Vincenzo Crupi

Journal of *Marine Science and Engineering*

MDPI

*Article*

# Design of an Innovative Hybrid Sandwich Protective Device for Offshore Structures

**Hozhabr Mozafari [1], Fabio Distefano [2], Gabriella Epasto [2,*], Linxia Gu [3], Emanoil Linul [4,*] and Vincenzo Crupi [2]**

[1] Department of Mechanical Engineering, University of Nebraska-Lincoln, Lincoln, NE 68588, USA
[2] Department of Engineering, University of Messina, 98166 Messina, Italy
[3] Department of Mechanical and Civil Engineering, Florida Institute of Technology, Melbourne, FL 32901, USA
[4] Department of Mechanics and Strength of Materials, Politehnica University Timisoara, 300222 Timisoara, Romania
* Correspondence: gabriella.epasto@unime.it (G.E.); emanoil.linul@upt.ro (E.L.)

**Abstract:** Lightweight foam sandwich structures have excellent energy absorption capacity, combined with good mechanical properties and low density. The main goal of this study is to test the application of an innovative hybrid sandwich protective device in an offshore wind turbine (OWT). The results are useful for offshore structure applications. Different lightweight materials (aluminum foam, agglomerated cork, and polyurethane foam) were investigated using experimental tests and numerical simulations. Closed-cell aluminum foam showed the best performance in terms of the energy absorption capacity during an impact. As such, a Metallic Foam Shell (MFS) device was proposed for the fender of offshore wind turbines. A finite element model of a ship-OWT collision scenario was developed to analyze the response of a fender with the MFS device under repeated impacts. The proposed MFS fender can be used efficiently in a wide temperature range, allowing it to be used in harsh climatic conditions.

**Keywords:** offshore structures; ship collision; aluminum foam sandwich; lightweight structures; finite element analysis; crashworthiness; safety of navigation



**Citation:** Mozafari, H.; Distefano, F.; Epasto, G.; Gu, L.; Linul, E.; Crupi, V. Design of an Innovative Hybrid Sandwich Protective Device for Offshore Structures. *J. Mar. Sci. Eng.* **2022**, *10*, 1385. https://doi.org/10.3390/jmse10101385

Academic Editor: Cristiano Fragassa

Received: 3 September 2022
Accepted: 23 September 2022
Published: 27 September 2022



## 1. Introduction

An overview on the current and future trends for marine applications of sandwich structures is provided by [1,2]. Among the different types of sandwich materials used for marine structures, aluminum materials offer some advantages in terms of weight reduction and environmental benefits. However, aluminum sandwich marine structures are subjected to complex loading conditions, so it is necessary to evaluate their responses under fatigue [3–5] and impact loading [6–12]. The effect of the adhesive on the impact response of adhesively bonded aluminum honeycomb sandwich panels was investigated in [13]. The hull structures could be subjected to slamming loads caused by repeated water impacts. The honeycomb core sandwich panels, the most widely used material for racing yacht hulls, were investigated in [14]. Aluminum honeycomb sandwich (AHS) structures were recently suggested as impact-absorbing structures to protect polar ships and marine structures from floating ice collisions [15,16].

Obviously, the application of aluminum sandwich structures requires an appropriate design procedure. The authors of [17] recently proposed a design procedure for AHS, which was further developed for the application of AHS as a replacement for the conventional steel inner side shell of the cargo hold of a bulk carrier [18].

As reported in [19], ship and offshore structures may frequently suffer from repeated impact loadings during their service life. This is due to different reasons, such as helicopters landing, ice floe impact, slamming on the bow, green water on the deck, sloshing and jet flow in liquefied natural gas (LNG) tanks, and collisions between supply vessels and

offshore platforms. Therefore, the structural safety of marine structures under repeated impact loads has attracted considerable attention [20,21]. Current studies of aluminum foam sandwich (AFS) panels are mainly concentrated on the mechanical response under a single impact; the behavior of these materials under repeated impacts has been only studied in few recent papers [6,22,23].

In the design of offshore structures, it is necessary to assess the collision resistance against ship impacts. Wind turbines are the main source of renewable energy. Offshore wind turbines (OWTs) offer some advantages with respect to onshore wind turbines in terms of energy production, the availability of large open spaces and fewer complaints about noise and the visual impact on the natural environment [24]. Additionally, the wind over the water is generally stronger, more consistent, and much smoother than that over land. Thus, OWTs produce, on average, 30% more energy than onshore turbines with the same installed power. However, OWTs are more expensive and difficult to install and maintain than onshore wind farms. OWTs are generally installed in regions with favorable wind conditions, ideally in the proximity of large ports. The offshore wind market has grown exponentially worldwide over the last decade. According to the Global Wind Report 2021 [25] by the Global Wind Energy Council (GWEC), i.e., the international trade association for the wind power industry, 2020 was the second-best year ever for the global wind power industry, with over 6 GW of new offshore installations and 35.3 GW of total installations, despite the impact of COVID-19. Nevertheless, a new report published by GWEC warned that the world needs to increase new wind power capacity three times more rapidly over the next decade to achieve global climate targets.

Nowadays, with the growth of OWT installations located close to traffic lanes for commercial and passenger ships, the probability of ship-OWT collisions is increasing, with severe consequences for the safety of navigation, ranging from structural damage to the collapse of the OWT support and the probable sinking of ships, environmental pollution and, at worst, the loss of human life. Additionally, the regular inspection and maintenance of OWTs requires the use of offshore supply vessels, bringing the risk that the vessels and the OWT will collide during the vessel berthing. For this reason, risk analyses for ship collision events have become a necessity. Hence, the collision of ships with OWTs has been widely treated in literature [19,26–32]. Many authors have applied finite element analyses (FEA) to overcome the difficulties of conducting experimental full-scale testing of ship collisions, which are expensive and requires a lot of time and manpower.

Considering the above issue, various crashworthy devices were proposed to absorb energy during the ship–OWT collisions. Liu et al. [27] proposed a crashworthy device containing a rubber blanket and outer steel shell to examine the impact of a ship on a monopile OWT. Qiu et al. [33] proposed a novel protective device composed of a buoyancy tank and a ring beam structure, and stated that the energy absorption effect can be improved using new sandwich panels. Han et al. [19] conducted nonlinear and dynamic FEA to investigate collisions between a 4 MW tripod OWT and a 2500 t ship. They compared the anti-collision performance of four types of fenders for OWT tripods. The fender consists of an outer steel shell and an internal bracket; the four types of fenders differ in terms of the materials used for the internal bracket, i.e., rubber, aluminum foam, rubber-aluminum foam, or aluminum foam-rubber. The results of the FEA demonstrated that aluminum foam is the best choice for the crashworthiness performance of the fender.

An innovative Foam-filled Lattice Composite Bumper System (FLCBS) with fiber-reinforced polymer (FRP) skins and a polyurethane foam-web core was proposed as a protective structure against ship collision for bridge piers [34]. Other authors proposed honeycomb structures to reinforce offshore platforms in case of collisions with ships [35].

The authors of [36] proposed an innovative protective device, i.e., a Metallic Foam Shell (MFS), composed of aluminum foam sandwich (AFS), to provide protection of railway vehicle axles against flying ballast impact. They demonstrated that the proposed device could absorb up to 90% of the initial impact energy, providing total protection to the axle.

Considering that impacts with OWTs can also happen in oblique directions, the use of a foamed core for the fender may be appropriate, as it usually has isotropic behavior. Moreover, a fender entirely made of aluminum, i.e., for both the skins and the core, has the advantage of being fully recyclable and highly sustainable. On the other hand, both porosity and thickness can be tailored according to the required mechanical performance. It is true that aluminum is more expensive than synthetic composites, but in case of damage, the fender can be repaired by welded or bolted joints.

The AFS can be considered an optimum choice for fenders for OWTs due to its good corrosion resistance [37,38]. Moreover, the metal matrix is made of AlSi10 alloy (10 wt.% Si and Al balanced), which can be considered a good compromise in terms of its manufacturing features [39] and corrosion behavior. It does not contain copper, which can promote corrosion of the foam [40]. It is worth mentioning that the high electrical conductivity of aluminum makes the AFS suitable for electrostatic coating methods.

The aim of this research is to test the application of the proposed MFS protective device in offshore structures against repeated impacts caused by ships. OWT structures are prone to collisions with ships by the bow, stern, or side, as reported in [35,41]. The present study considers only a collision between an OWT and a ship bow.

The mechanical responses of different lightweight materials (aluminum foam, agglomerate cork, and polyurethane foam) under impact loading were obtained by experimental tests and used to validate the FE analyses. A preliminary FE model of AFS under single and repeated impacts was validated by means of experimental data, obtained by low velocity impact (LVI) tests. Then, the FE model of a ship–OWT collision scenario was validated by means of data reported in literature. Finally, the FE model was developed to simulate the responses of an OWT with the MFS protective device under repeated impacts from a ship bow.

## 2. Materials and Methods

An experimental investigation was carried out on the following lightweight materials: aluminum foam (AF), agglomerated cork (AC) and polyurethane foam (PUF). The investigated materials are shown in Figure 1. The AF was made by the powder metallurgical method. AlSi10 (10 wt.% Si and Al balanced) was used as a metal matrix and $TiH_2$ (0.4 wt.%) as a foaming agent. The manufactured AF was characterized by closed pores with an average size in the range of 2.5 to 3.5 mm. Pore-size distribution varied as follows: in the central area of the samples, the largest pores occurred (up to 4.5–5.5 mm), while in the upper and lower parts, where the skin is formed (thickness between 0.11–0.25 mm), they were in the order of 0.5 mm (isolated even smaller).

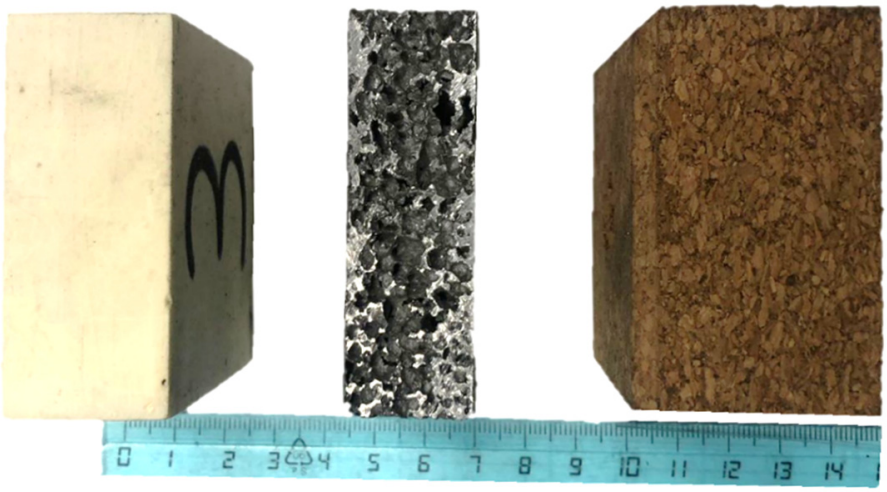


**Figure 1.** Investigated materials: PUF (**left**), AF (**middle**) and AC (**right**).

Compressive and low velocity impact tests were performed. Quasi-static compression tests were performed using an A009 (TC100) electromechanical computerized universal testing machine, equipped with a load cell of 100 kN. Tests were carried out under displacement control at a constant crosshead displacement of 10 mm/min and at room temperature (25 °C).

The low velocity impact (LVI) tests were performed with a Ceast Fractovis Plus drop test machine, equipped with a system for avoiding the multiple impacts. The impactor, instrumented by a 90 kN piezoelectric force transducer to record the force signal, had a conical shape with a diameter of 25.4 mm at the base and 12.7 mm at the tip. The drop test machine was equipped with a photocell that triggered the digital acquisition system at the passage of the impactor and measured its velocity ($v_0$) at the beginning of contact but before impact. The LVI tests were carried out at values of impact energy ranging from 15 to 35 J some panels of the investigated lightweight materials.

## 3. Results and Discussions

### *3.1. Experimental Tests*

Figure 2 shows the compressive stress-strain and energy absorption-strain curves. All curves highlighted the same pattern, and Figure 2 illustrates the most representative ones from each category (AF, PUF and AC).

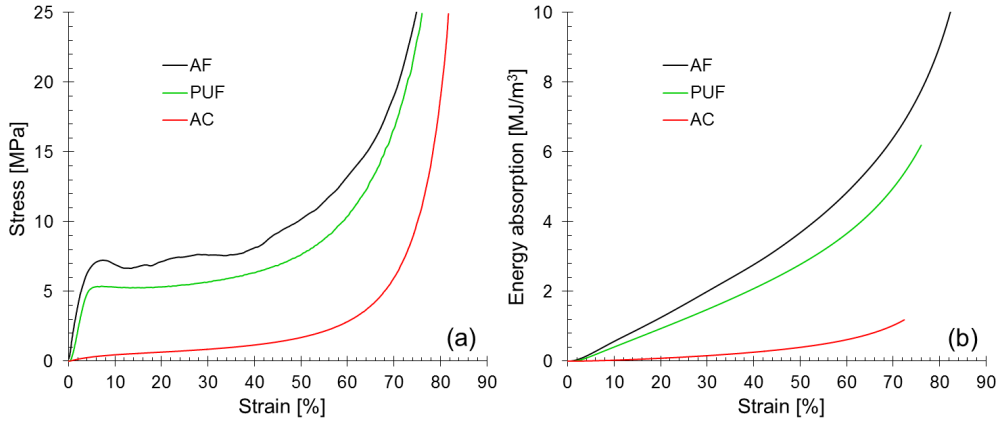


**Figure 2.** Compressive stress-strain (**a**) and energy absorption-strain (**b**) curves of AF, PUF and AC.

The stress-strain curves of the cellular materials show three zones. In the first, the stress-strain response is linear-elastic. The AF and PUF specimens have a clear peak stress at the end of this zone, and a sudden drop in the stress is observed for AF after experiencing the first maximum stress. In contrast to the foams, the AC samples show a lower initial slope with a smooth transition to the next zone, while the yield point cannot be easily identified. The compressive yield stress was highest for AF, followed by PUF and AC. The last zone is characterized by a high increment of stress. The results of the compressive tests for each material type were determined according to the ISO 13314-11 [42], ISO 844-21 [43] and ASTM D 1621-00 [44] standards and are presented in Table 1. Table 1 shows the average values with the standard deviations, obtained by three tests.

**Table 1.** Results of the quasi-static compressive tests.

| Sample Type | Compressive Modulus [MPa] | Compressive Strength [MPa] | Plateau Stress [MPa] | Densification Strain [%] | Densification Stress [MPa] | Energy Absorption [MJ/m$^3$] |
|---|---|---|---|---|---|---|
| AF | 183.56 ± 10.03 | 7.24 ± 0.04 | 7.63 ± 0.06 | 48.87 ± 0.11 | 9.92 ± 0.08 | 3.69 ± 0.04 |
| PUF | 176.57 ± 17.08 | 5.87 ± 0.83 | 5.83 ± 0.04 | 49.79 ± 0.07 | 7.58 ± 0.18 | 2.77 ± 0.04 |
| AC | 7.94 ± 0.17 | 0.65 ± 0.01 | 0.90 ± 0.07 | 40.45 ± 0.18 | 1.18 ± 0.04 | 0.40 ± 0.05 |

Even though they have different matrices (metal and polymer), the foams have approximately the same elastic property, with a difference of only 3.81% in favor of AF. The AC has a compressive modulus over 22 times lower than the foams. The major distinction between all three configurations becomes evident for strains greater than 7%, namely, the plateau zone. The densification strain was quite similar, presenting differences of maximum 17% among the tested samples. The samples showed the best energy absorption performance in the plateau area, because this is the most extensive. At the same time, the main collapse mechanisms of the cellular materials subjected to compression took place in this area. Figures 3–5 show the load-displacement curves obtained by the low-velocity impact tests.

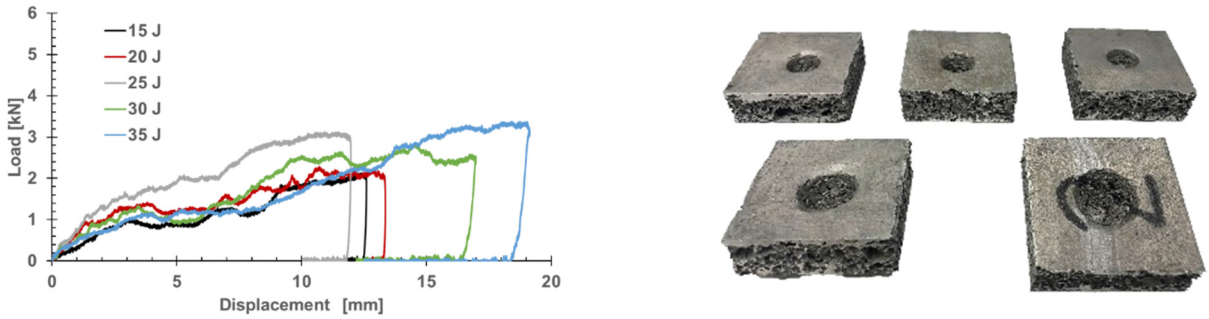


**Figure 3.** Load-displacement curves (**a**) and damaged AF panels (**b**) with thickness t ≈ 20 mm.

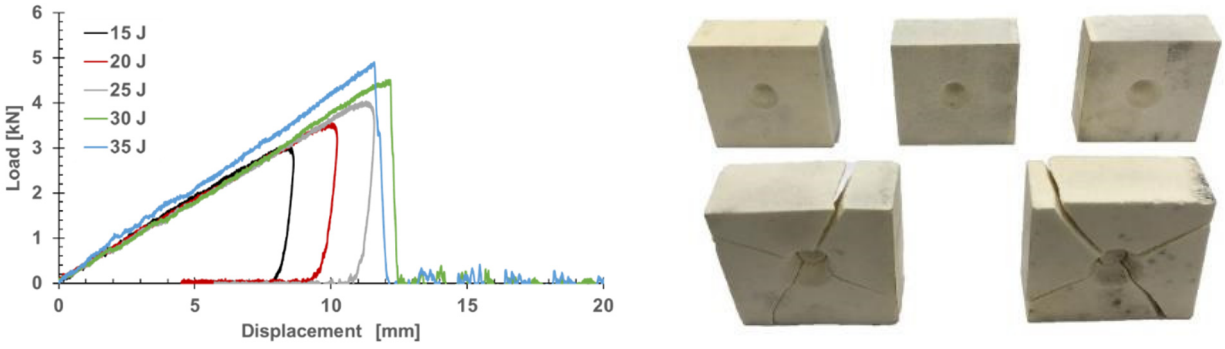


(**a**) (**b**)

**Figure 4.** Load-displacement curves (**a**) and damaged PUF panels (**b**) with thickness t ≈ 25 mm.

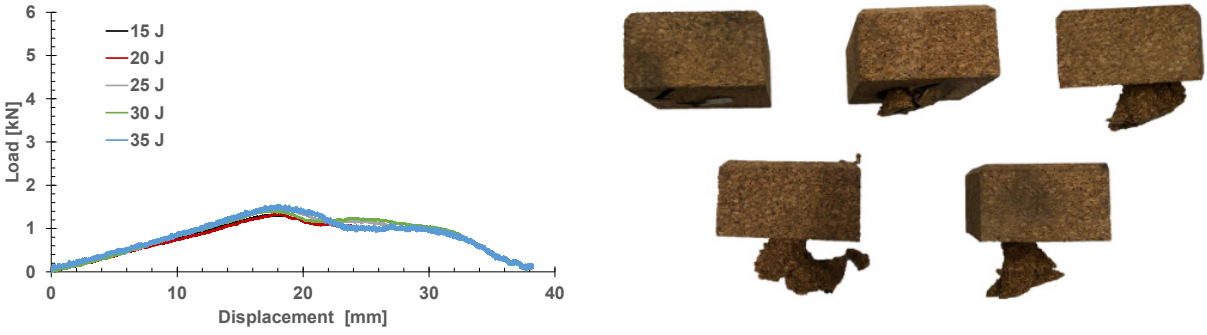


(**a**) (**b**)

**Figure 5.** Load-displacement curves (**a**) and damaged AC (**b**) panels with thickness t ≈ 35 mm.

Table 2 reports the impact energy ($E_i$), the mass (m), the dimensions of the panels (length l, width b, thickness t), the density (ρ), and the results of the LVI tests. The results are reported in terms of peak crush force ($F_{MAX}$) and depth (w), which are defined as the highest values of force magnitude and displacement observed in the force–displacement

curve. The specific absorbed energy (SAE) and the specific weight absorbed energy ($SAE_w$), which were calculated by dividing the amount of energy absorbed during the impact event ($E_a$) by the density ($\rho$) and the mass (m) of each specimen, are described in the Equations (1) and (2) below.

$$SAE = \frac{E_a}{\rho} = \frac{\int_0^w Fds}{\rho} \quad (1)$$

$$SAE_w = \frac{E_a}{m} = \frac{\int_0^w Fds}{m} \quad (2)$$

**Table 2.** Results of the impact tests.

| Material | $E_i$ [J] | m [g] | t [mm] | l [mm] | b [mm] | ρ [kg/m$^3$] | $F_{MAX}$ [kN] | w [mm] | SAE [Jm$^3$/kg] | $SAE_w$ [J/kg] |
|---|---|---|---|---|---|---|---|---|---|---|
| AF | 15 | 32.49 | 19.57 | 60.72 | 60.51 | 451.84 | 2.12 | 12.60 | 0.033 | 461.7 |
| AF | 20 | 32.68 | 20.31 | 60.65 | 60.58 | 438.00 | 2.29 | 13.38 | 0.046 | 612.0 |
| AF | 25 | 31.76 | 20.12 | 60.68 | 60.59 | 429.39 | 3.13 | 11.97 | 0.058 | 787.2 |
| AF | 30 | 33.16 | 20.05 | 60.43 | 60.42 | 452.98 | 2.84 | 16.98 | 0.066 | 904.7 |
| AF | 35 | 31.98 | 19.98 | 60.53 | 60.49 | 437.12 | 3.38 | Perforated | 0.078 | 1068.2 |
| PUF | 15 | 28.86 | 25.28 | 60.86 | 60.69 | 309.11 | 3.05 | 8.62 | 0.049 | 519.8 |
| PUF | 20 | 28.62 | 25.32 | 60.74 | 60.65 | 306.80 | 3.55 | 10.23 | 0.065 | 698.8 |
| PUF | 25 | 28.62 | 25.26 | 60.73 | 60.49 | 308.45 | 4.04 | 11.59 | 0.081 | 873.5 |
| PUF | 30 | 28.51 | 25.34 | 60.78 | 60.59 | 305.47 | 4.51 | Perforated | 0.091 | 972.6 |
| PUF | 35 | 28.48 | 25.25 | 60.68 | 60.22 | 308.65 | 4.91 | Perforated | 0.093 | 1010.2 |
| AC | 15 | 33.27 | 34.97 | 64.29 | 59.20 | 249.94 | 1.32 | 18.39 | 0.060 | 450.9 |
| AC | 20 | 32.21 | 35.04 | 64.31 | 59.10 | 241.89 | 1.35 | 24.02 | 0.083 | 620.9 |
| AC | 25 | 32.74 | 34.94 | 64.32 | 58.27 | 250.01 | 1.49 | Perforated | 0.098 | 746.0 |
| AC | 30 | 34.18 | 34.91 | 63.87 | 59.24 | 258.73 | 1.40 | Perforated | 0.097 | 731.4 |
| AC | 35 | 31.82 | 34.44 | 64.27 | 57.96 | 248.03 | 1.55 | Perforated | 0.101 | 786.2 |

A lower $F_{MAX}$ and a higher SAE are optimal for the crashworthiness of a structure. As reported in Table 2, perforation of the panels was observed at the following impact energies: 25 J for AC, 30 J for PUF and 35 J for AF.

PUF panels presented the highest $F_{MAX}$ (Table 2). Figure 4b shows the PUF panels after the impact tests. They showed a brittle fracture, which is confirmed in the load-displacement curves by the abrupt load drop after achieving the $F_{MAX}$, as shown in Figure 4a. This brittle failure is a critical point for their application.

The specimens made of AC had a higher thickness compared to the PUF and AF specimens, and this parameter influenced the impact response. As shown in Table 2, the AC specimens presented the lowest $F_{MAX}$ and the highest SAE, which is the optimal solution for crashworthiness. However, the lowest value of impact energy (25 J) for producing the perforation of the panel also occurred with AC specimens.

Despite AF panels presenting the highest density values (Table 2), they had the highest value of impact energy (35 J), which caused perforation of the panel, and their failure mode was characterized by the densification of the core, which allowed them to absorb more energy during the impact. From the analysis of LVI tests results, it was found that AF represented the optimal solution among the tested materials for application as a protective device for offshore structures.

### *3.2. Finite Element Analyses of Lightweight Panels under Single and Multiple Impacts*

FE models of the low velocity impact test were generated using Abaqus Software. The Abaqus/Explicit solver was implemented to simulate the low velocity impacts. The FE model was composed of the impactor, the panel, and the base, which was comprised an analytical rigid body. The impactor considered in the FE model had the same shape and dimensions as the one used for the LVI tests. After a mesh sensitivity analysis, the panel was meshed with 2 mm solid elements.

The following materials were considered for the panels in the FE analyses: AF, AC, PUF. The panels of the investigated lightweight materials had the dimensions shown in Table 2. The same value of impact energy (35 J) as that applied for LVI tests was considered for FEA. Various constitutive models have been suggested in the literature over the last decade for numerical simulations of metallic foams under impact loading. According to a previous published paper, the Crushable Foam Plasticity with Ductile Damage Abaqus criterion was applied for AF [45]. The same material model was implemented for AC. The PUF was modelled as a brittle elastic material because the response of the PUF under impact was linear to the point of failure.

Two main mechanisms can cause the fracture of a ductile metal: ductile fracture due to the nucleation, growth, and coalescence of voids, or shear fracture due to shear and band localization. Based on phenomenological observations, these two mechanisms call for different criteria for the onset of damage [46]. Abaqus provides the functional forms for these criteria, which can be used for damage evolution models for ductile metals to simulate ductile fractures of a metal.

The ductile criterion model assumes that the equivalent plastic strain at the onset of damage $\bar{\varepsilon}_D^{pl}$ is a function of stress triaxiality and strain rate $\bar{\varepsilon}_D^{pl}\left(\eta\check{\varepsilon}^{pl}\right)$, where $\eta = -p/q$ is the stress triaxiality, $p$ is the pressure stress, $q$ is the Mises equivalent stress, and $\check{\varepsilon}^{pl}$ is the equivalent plastic strain rate. The criterion of damage initiation is met when the following condition is satisfied:

$$\omega_D = \int \frac{d\bar{\varepsilon}^{pl}}{\bar{\varepsilon}_D^{pl}\left(\eta, \check{\varepsilon}^{pl}\right)} = 1 \tag{3}$$

where $\omega_D$ is a state variable that increases monotonically with plastic deformation. At each increment during the incremental increase, $\omega_D$ is computed as

$$\Delta\omega_D = \frac{\Delta\bar{\varepsilon}^{pl}}{\bar{\varepsilon}_D^{pl}\left(\eta, \check{\varepsilon}^{pl}\right)} \geq 0 \tag{4}$$

The ductile criterion can be used in conjunction with the Mises plasticity model in the Abaqus Explicit solver. Based on the stress-strain curves that were obtained for AF and AC, the plastic behavior and the yield strength at the onset of damage were extracted. As observed from the impact tests, PUF presented a brittle failure mode, so we used Brittle Failure Criterion in Abaqus to simulate that behavior. According to the model, when one, two, or all three local direct cracking strain or displacement components at a material point reach the value defined as the failure strain $\left(e_{nn}^{ck}\right)_f$ or displacement $\left(u_n^{ck}\right)_f$, the material point fails, and all the stress components are set to zero. If all the material points in an element fail, the element is removed from the mesh. The initiation of progressive failure for PUF was set equal to the initiation of the second zone of the compressive stress-strain curve (Figure 2). The failure strain, used in this FE modelling as failure criteria, was set to 0.001.

Regarding boundary and loading conditions, the impactor was constrained in all Degrees of Freedom (DOFs), but not in the axial direction. An initial velocity was applied to the striker to simulate a low-velocity impact. A symmetric boundary condition was applied to the lateral faces of the sandwich panel. The out-of-plane constraint was applied to the bottom of the sandwich panel to simulate the support plate used in the experimental tests. The element removal capability of Abaqus was used to leave out the failed elements from the damaged model.

The stress-strain curves, obtained by the compressive tests for the investigated materials, were used as input parameters in the FE models. The obtained results were compared with the experimental tests, as shown in Figures 6 and 7.

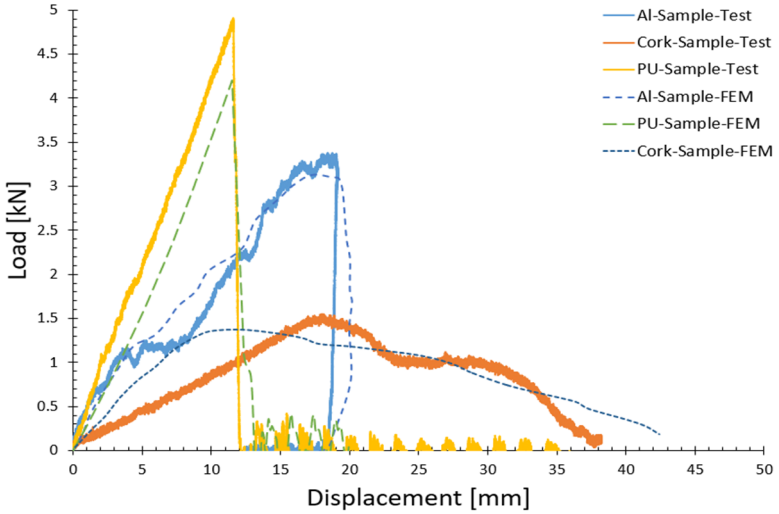


**Figure 6.** Experimental and FE load-displacement curves from the impact tests.

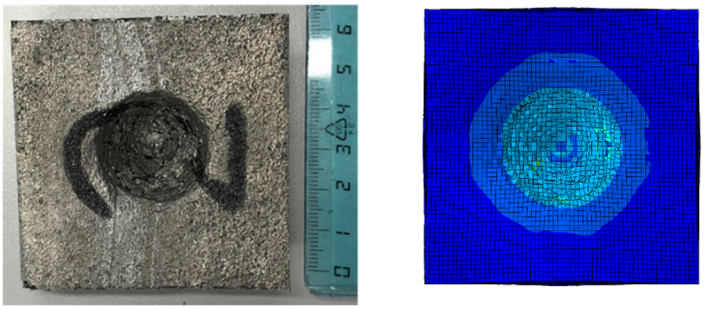

Aluminum Foam

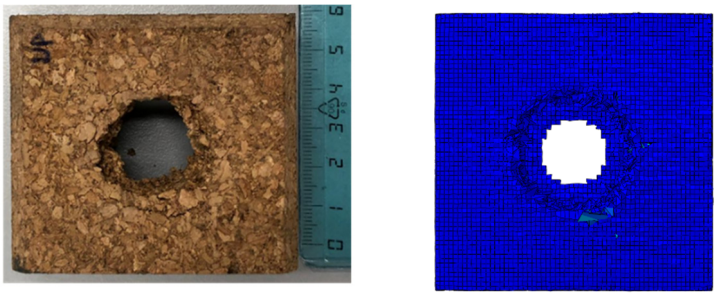

Agglomerated Cork

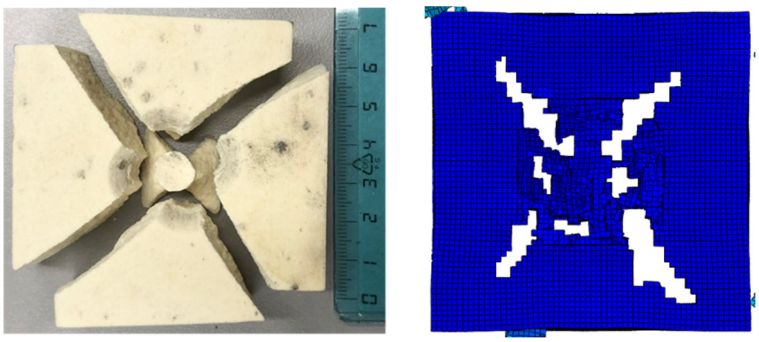

PU Foam

**Figure 7.** Comparison between experimental (**left**) and FE (**right**) damaged samples after impacts.

The response of AF and AC is ductile, with more energy absorption than PUF. On the other hand, PUF takes the impact load via a sharp increase of reaction load until cracking and failure occurs.

The FE models were able to predict the mechanical response of the samples with less than 10% variation of the maximum load.

The FE model of the AFS panels was developed to investigate their response under single and multiple impact tests, and the FE results were compared with the experimental data reported in previous studies by the present authors [6,36].

The load displacement curves from the FE analyses and experimental results showed a similar trend. For all the configurations, load fluctuations were present along the curves, the impact energy was fully absorbed, since the load values returned to zero, and the curves were closed. A comparison of the FE results with the experimental data is reported in Table 3.

**Table 3.** Comparison between the simulated impact tests results and the experimental results.

| | $F_{MAX}$ [N] | $F_{MAX}$ Error [%] | w [mm] | w Error [%] |
|---|---|---|---|---|
| L-34-AFS-EXP | 5934.4 | 5.12 | 7.4 | −8.11 |
| L-34-AFS-FEA | 6238.1 | | 6.8 | |
| M-34-AFS-EXP | 7567.2 | 9.79 | 5.8 | −5.17 |
| M-34-AFS-FEA | 8308.4 | | 5.5 | |
| H-34-AFS-EXP | 8936.7 | −1.62 | 4.8 | 8.33 |
| H-34-AFS-FEA | 8791.6 | | 5.2 | |

For both the experimental and numerical results, the peak force $F_{MAX}$ increased while depth w decreased with increasing of the core density. The FE results were in good agreement with the experimental data; the percentage error values of peak force $F_{MAX}$ and depth w were all lower than 10%.

The peak force and depth errors for the repeated impact test are reported in Table 4.

**Table 4.** Comparison between the repeated impact tests FE results and the experimental results.

| | $F_{MAX}$ [N] | $F_{MAX}$ Error [%] | w [mm] | w Error [%] |
|---|---|---|---|---|
| AFS-I-EXP | 5934.4 | −1.77 | 7.4 | 5.6 |
| AFS-I-FEA | 5829.5 | | 7.01 | |
| AFS-II-EXP | 7982.7 | 0.25 | 5.7 | 7.9 |
| AFS-II-FEA | 8002.7 | | 6.19 | |
| AFS-III-EXP | 9399.0 | 0.35 | 5.4 | 0.7 |
| AFS-III-FEA | 9431.8 | | 6.36 | |

For both the FE and experimental results, the peak force increased after each impact, and small percentage errors were detected with values lower than 2%. In the experimental tests, the depth values decreased after each impact due to core crushing and densification. Good agreement in the depth results was detected for all impact tests, with percentage errors lower than 10%. The total depth after three impact tests for FEA and experimental results was very similar.

The skin was meshed with solid elements considering four elements through the thickness of the skin, i.e., 2 mm, in order to accurately capture the bending response. The skins were made of aluminum alloy AA6082, which has the following mechanical properties [47]: density $\rho$ = 2700 kg/m$^3$, tensile strength $\sigma_y$ = 370 MPa, ultimate stress $\sigma_u$ = 385 MPa, modulus of elasticity E = 70 GPa, total elongation at fracture $\varepsilon_{max}$ = 10%. Three values of core density were considered: 490 kg/m$^3$ (specimen L-34-Al), 570 kg/m$^3$

(specimen M-34-Al), 690 kg/m$^3$ (specimen H-34-Al). The stress-strain curves of AlSi10 aluminum alloy foam, as used in the FE model, were obtained from quasi-static compression tests [10]. The skin was tied to the upper face of the core, and a surf-surf contact Abaqus option was defined between the impactor and the skin. A general type of contact between all the elements of the aluminum core against the skin was defined. As such, if the first layer of elements failed, then there would be still a contact interaction between the second layer of elements and the skin.

The load–displacement curves of the AFS panels, obtained by FEA, were compared with the experimental curves, obtained by LVI tests [36] for three samples, as shown in Figure 8. The AFS specimens had aluminum skins and an aluminum foam core with a thickness of 34 mm. They differed in terms of core density, and as such, they have the following codes: L-34-Al (ρ = 490 kg/m$^3$), M-34-Al (ρ = 570 kg/m$^3$), H-34-Al (ρ = 690 kg/m$^3$). The FE results were in good agreement with the experimental data.

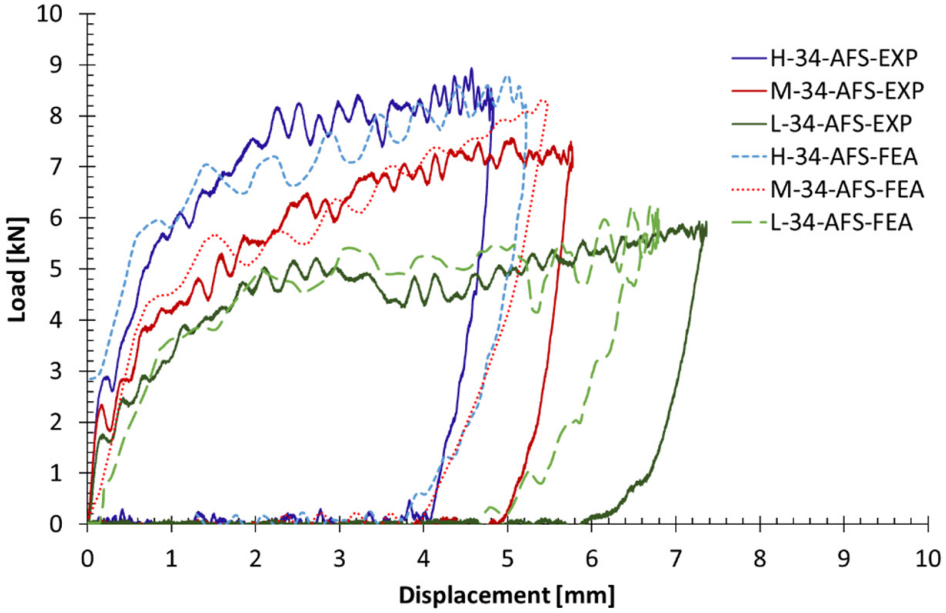


**Figure 8.** FE and experimental load-displacement curves of the aluminum sandwich panels.

The FE model was modified to simulate multiple impacts: two other impactors were imported in the assembly to have total of three impacts. The energy of each impact was equal to 35 J. Figure 9 shows the FE results of the sandwich panel for the three impacts. The progressive damage through the core of the sandwich panel that contributed to the load-displacement fluctuation was captured.

The multi-impact responses of PUF and AC sandwich (PUFS and ACS) panels were modelled as well. The load–displacement curves of the panels after the three impacts, obtained by FEA, are shown in Figure 10. The stiffness of the AFS panel increased after each impact. Interestingly, the ACS panel showed less enhancement in reaction force after each impact. The responses for the PUFS panel were slightly different. As the PUFS panel absorbed the impact energy, some cracks initiated and grew until the complete fracture of the panel. The drop force due to the brittle fracture properties of PUFS is shown in Figure 10.

Figure 11 shows the load–displacement curves for AFS panels subjected to 10 impact tests, including stages of loading and unloading at an impact energy of 35 J. The experimental curves were obtained by LVI tests [6]. A comparison between the FE curves in Figure 10 and the experimental curves in Figure 11 demonstrates that the FE results for AFS under multiple impacts are in good agreement with the experimental data.

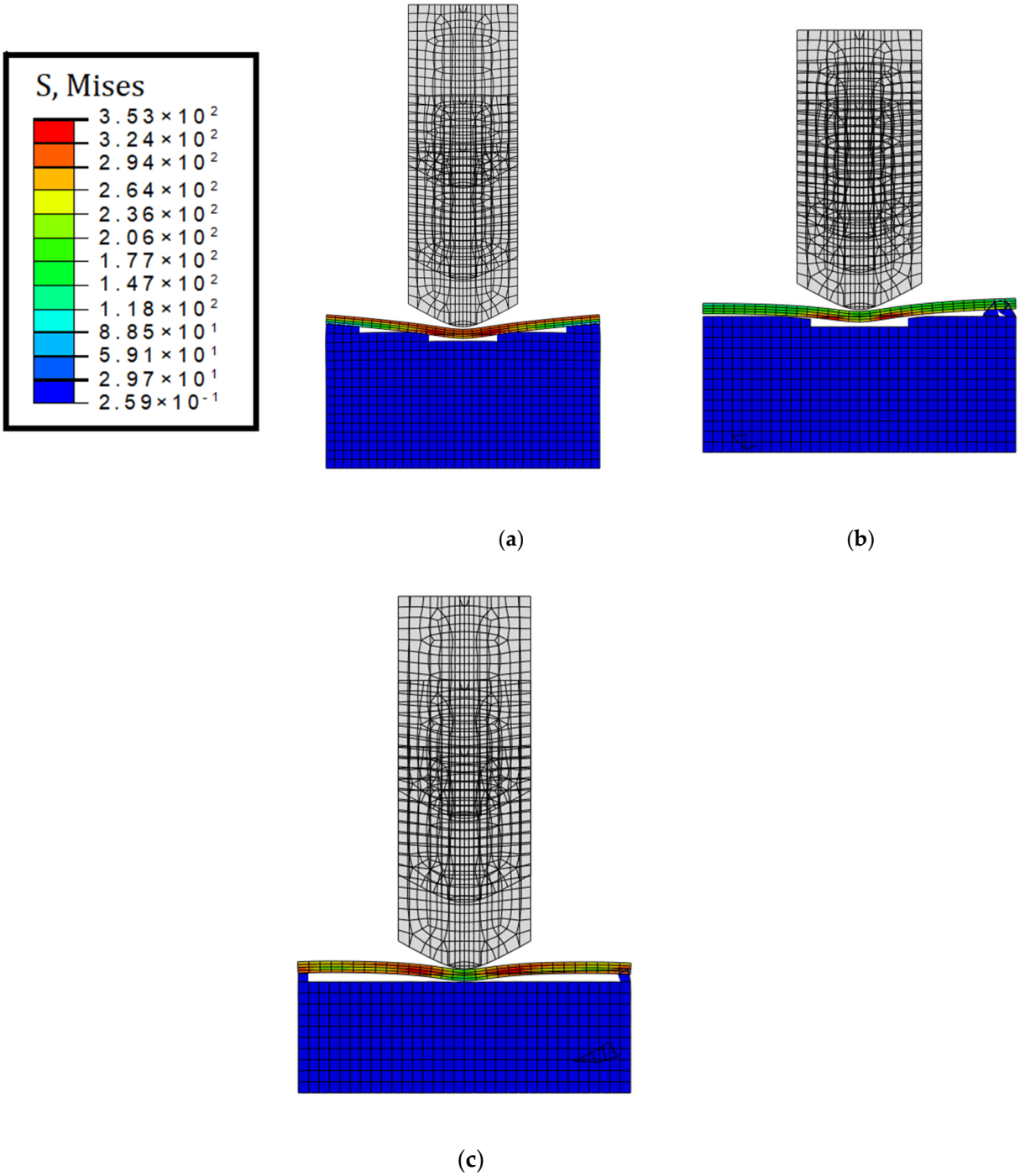


**Figure 9.** FE Von Mises stresses after multiple impacts. (**a**) 1st impact; (**b**) 2nd impact; (**c**) 3rd impact.

### *3.3. Finite Element Analyses of Ship Bow-OWT Collision Scenario*

OWTs consist of a support structure or foundation, a main column or tower, a fender, a nacelle, a hub, the blades, and an electrical system. The most widely used types of OWT foundations are the following: the monopile, suitable for water depths of 18–25 m; the jacket, generally installed for water depths of 20–50 m; and the tripod, which is more suitable for deep-sea areas than the monopile or the jacket. The collision scenario, investigated in the FE model, considered the impact of a ship bow against an innovative fender of a tripod OWT.

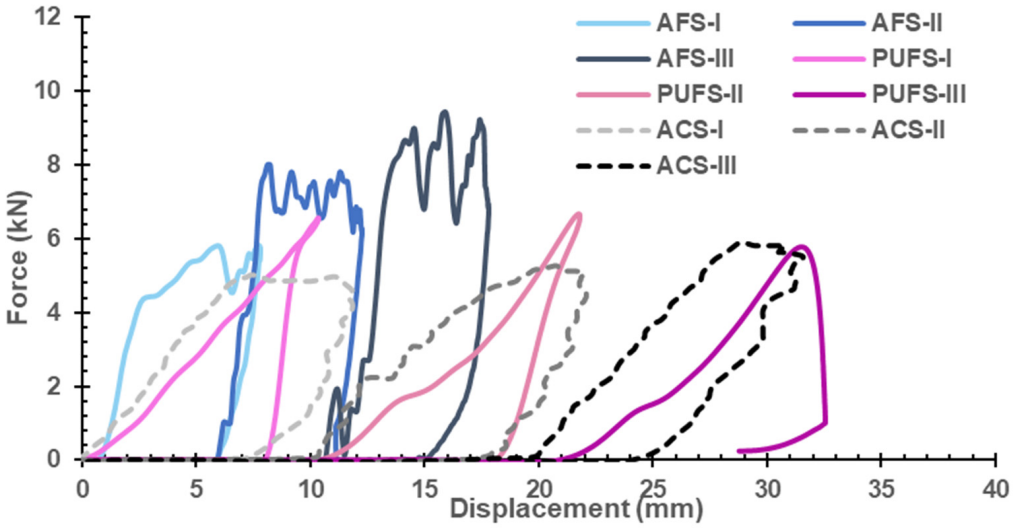


**Figure 10.** FE load–displacement curves of each impact for the multi-impact simulation.

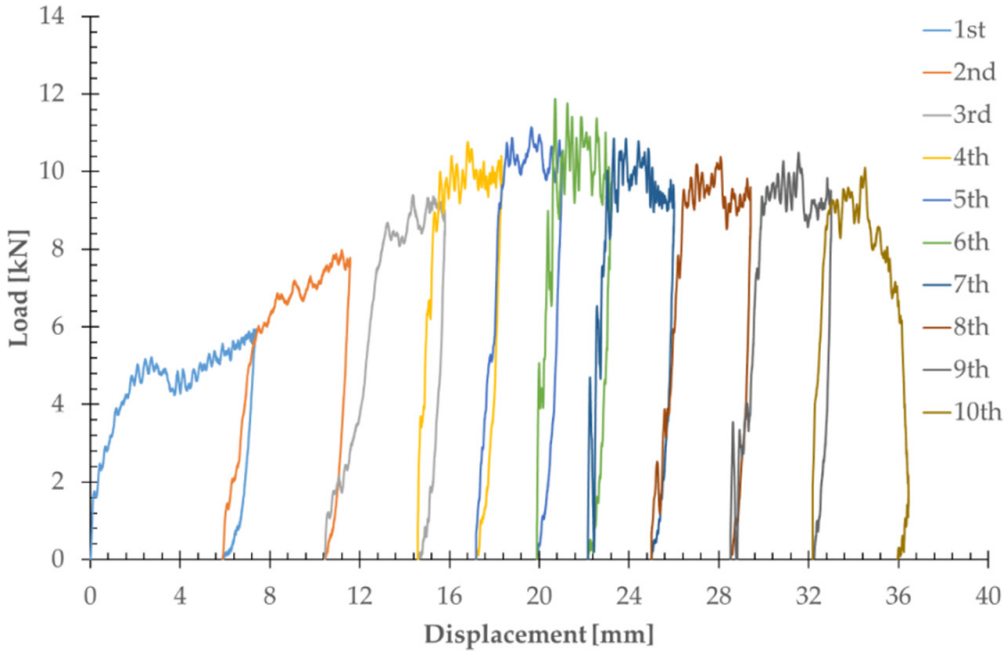


**Figure 11.** Experimental curves for AFS panel subjected to repeated impacts at impact energy equal to 35 J [6].

The FE model applied in this study was similar to one reported in the literature [19]. The collision occurred between the OWT fender and the ship bow. The OWT consisted of a main column, lateral and horizontal braces, and pipe columns to hold the structure in the ocean. Only the ship bow was considered in the FEA, as the rest of the ship does not make significant contribution to collisions, notwithstanding its mass. Hence, a reference point was assigned to the bow with a total mass of 2500 t in order to include the ship displacement. The fender, installed in the base center with a length of 14 m and total thickness of 1.4 m, was made of inner rubber and outer aluminum foam. The isotropic hyperelastic material model was chosen based on the strain-energy density function using the Odgen form [19]. The bow was modelled using Q235 steel properties, while the wind turbine structure and its foundation were made of Q 345 steel. The mechanical properties of these parts can be found in [19].

The OWT was meshed with solid linear elements, with finer elements in the impact area (0.2 m), to capture the accurate response and larger elements (0.6 m) on the other sections in order to enhance the computational efficiency. The bow was meshed with shell elements. Figure 12 shows the FE model of the OWT-ship collision scenario.

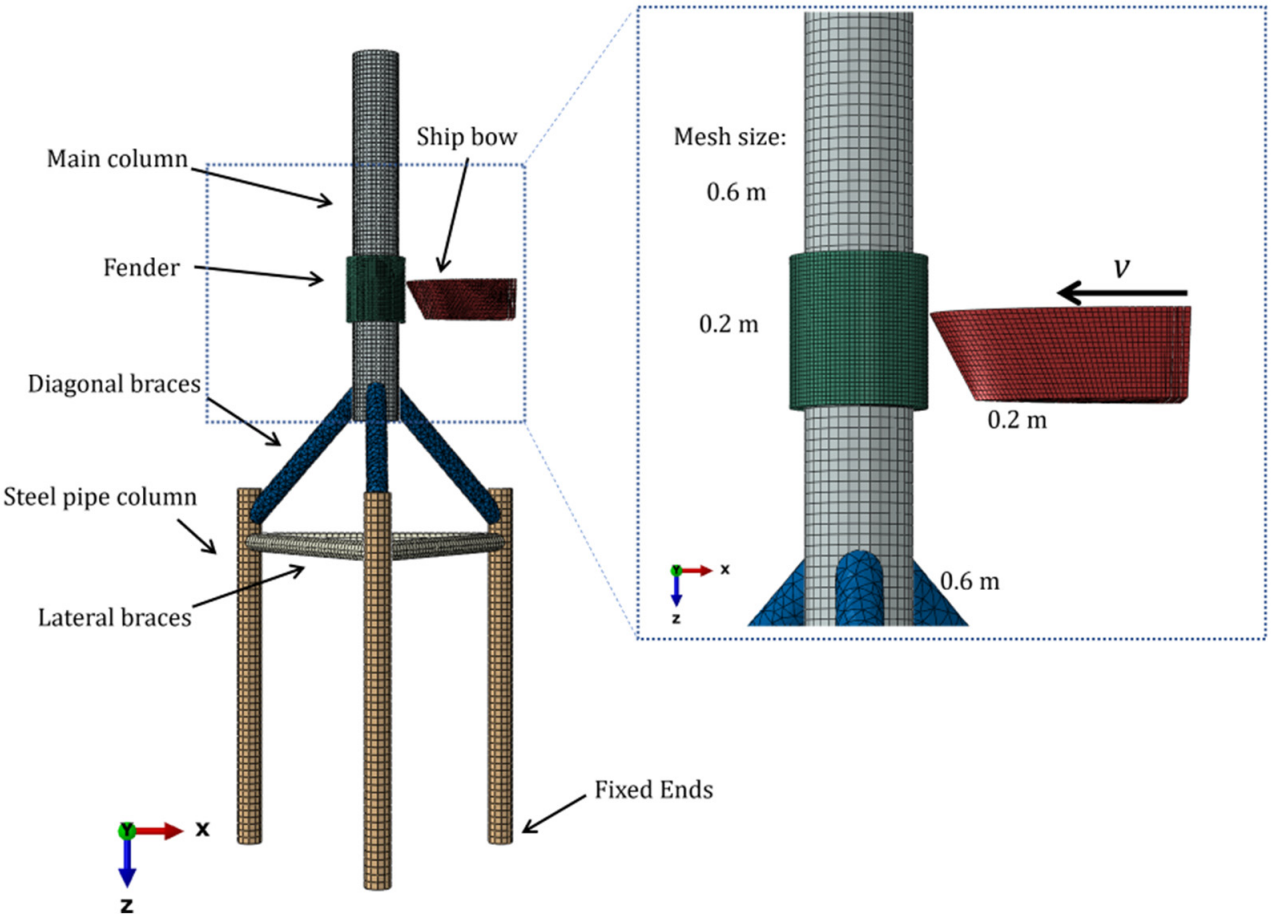


**Figure 12.** FE model of OWT-ship collision.

Surface-to-surface contact was created between the bow and the fender. A tie constraint was applied to couple the DOFs of the OWT components at their interface. In the collision scenario, the impact velocity of the ship was equal to 2 m/s.

The collision of the ship bow against the OWT was simulated under single and multiple impact scenarios. In the first step, the FE model was compared with the one developed by Han et al. [19]. Figure 13 shows the load-time responses of the OWT with and without the aluminum foam fender, demonstrating the advantage of the use of an aluminum foam fender in sandwich configuration.

The results show that the FE model correctly predicted the trend of energy absorption in both cases. Additionally, there was around 15% difference between this model and the one developed by Han et al. [19]. This difference may have stemmed from the higher impact energy included in this FE model. In their model, a linear elastic foundation with a damping system that represented different layers of soil (Soil-pile model) was used. In our model the seabed was simplified using a tie constraint at the end of vertical piles of OWT, so the rigidity of the boundary condition, and subsequently, the recorded reaction forces, increased due to the impact. The main reason to modify the boundary condition was to build a computationally efficient model that could be used to conduct a comparative study on different configurations for the fender.

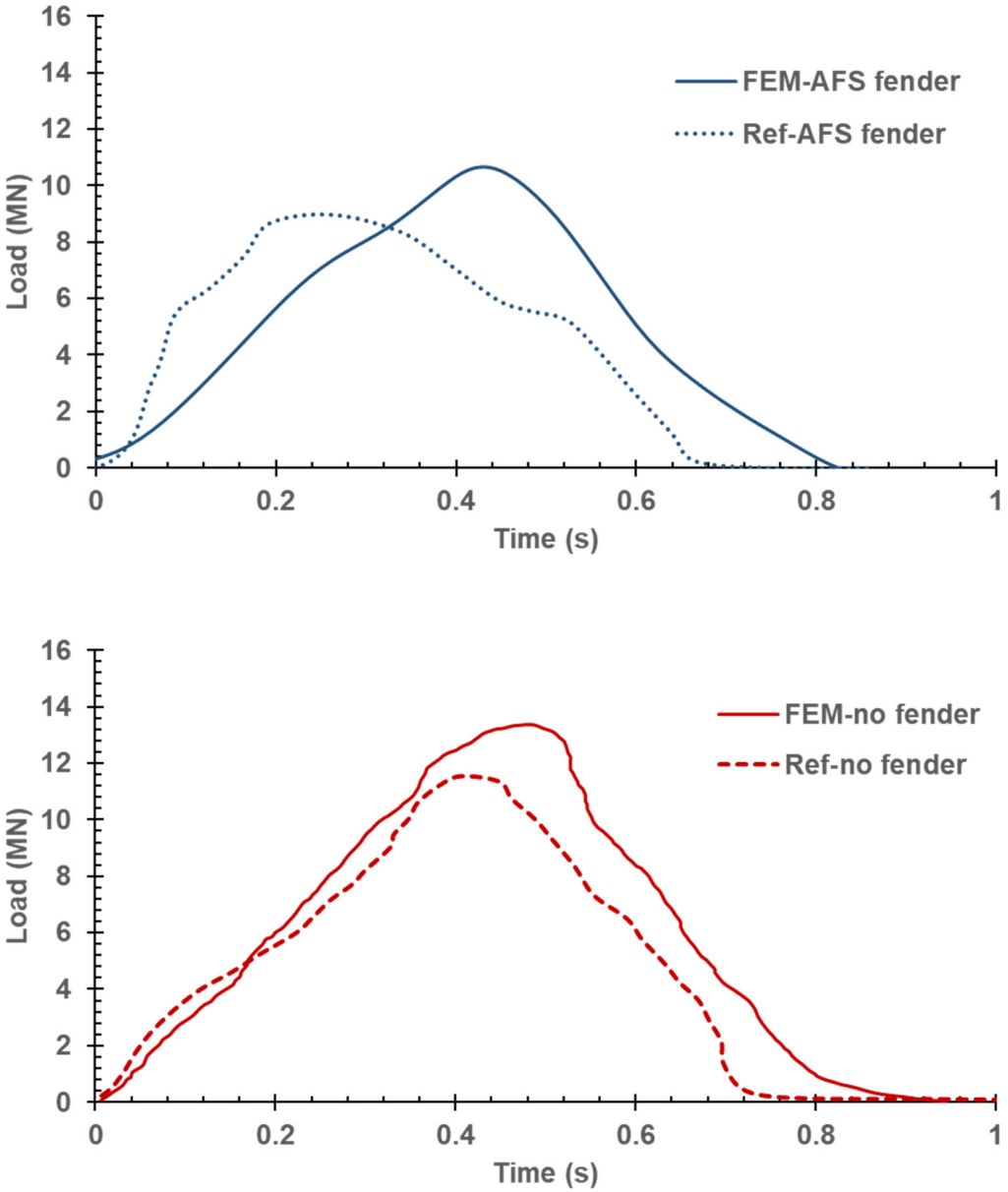


**Figure 13.** Load-time of the single impact collision and comparison with [19] of the OWT with and without AFS fender.

Figure 14 shows the stress distribution of the OWT due to the impact of a ship bow for different fenders with AF, AC, and PUF sandwich panels (AFS, ACS and PUFS, respectively). AFS absorbed the greatest amount of impact energy and transferred less stress to the OWT structure. The maximum stress recorded at the lower end of the diagonal braces in the case of AFS was 15 MPa, while this parameter was 20 MPa and 22 MPa for the ACS and PUFS, respectively. Interestingly, the stress distribution around the location of impact differed in each case. The AFS fender successfully mitigated the stress field from the rest of structure, and the value of maximum stress, 12 MPa, was captured on the main column at the location of fender. However, using an ACS fender, the stress value at this location increased to 15 MPa. The highest magnitude of relevant stress was observed with the PUFS fender (19 MPa).

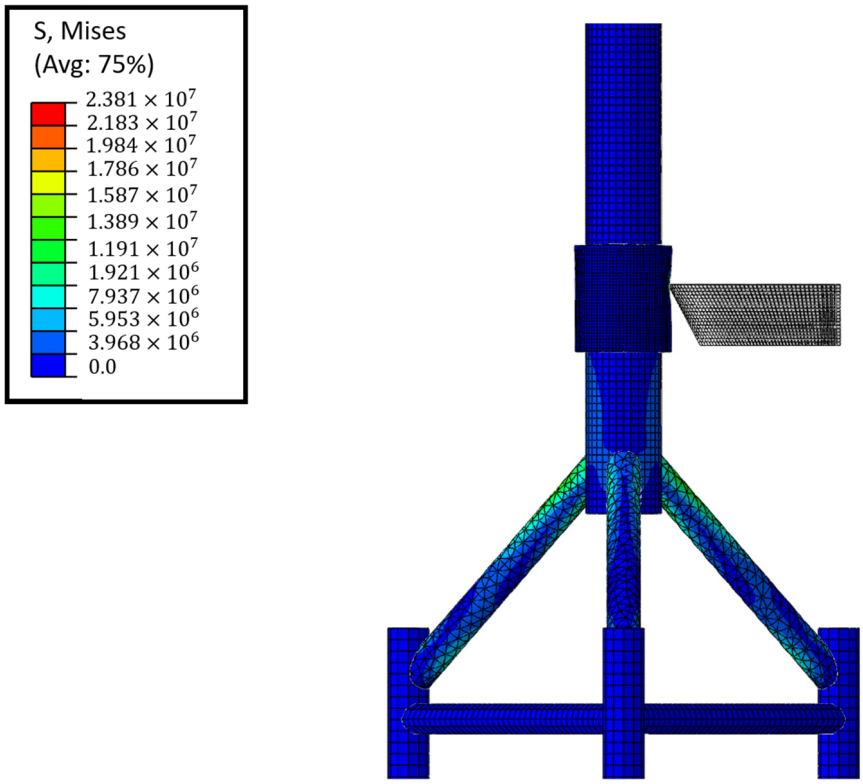


(**a**)

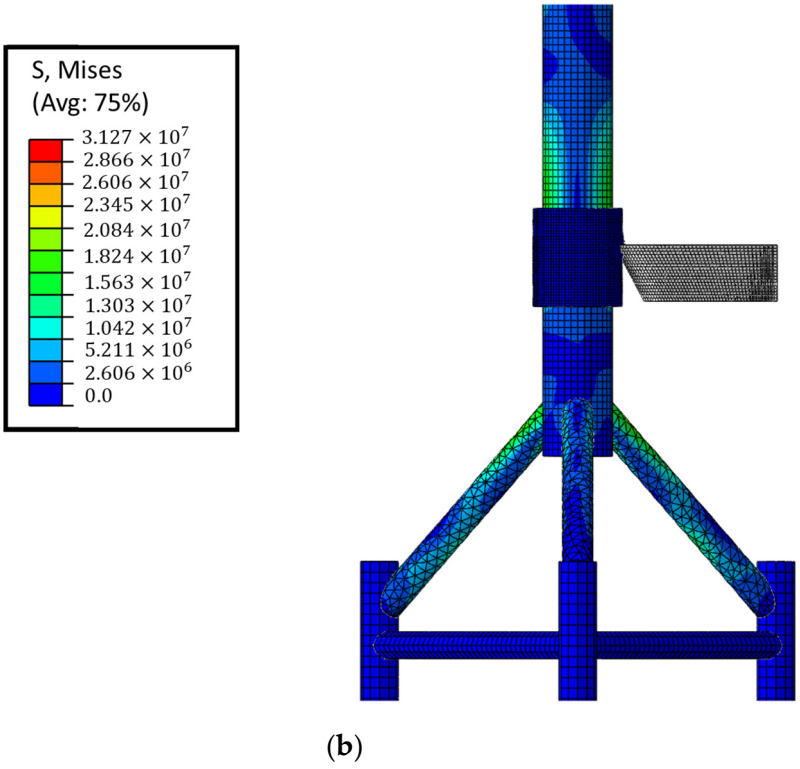


(**b**)

**Figure 14.** *Cont.*

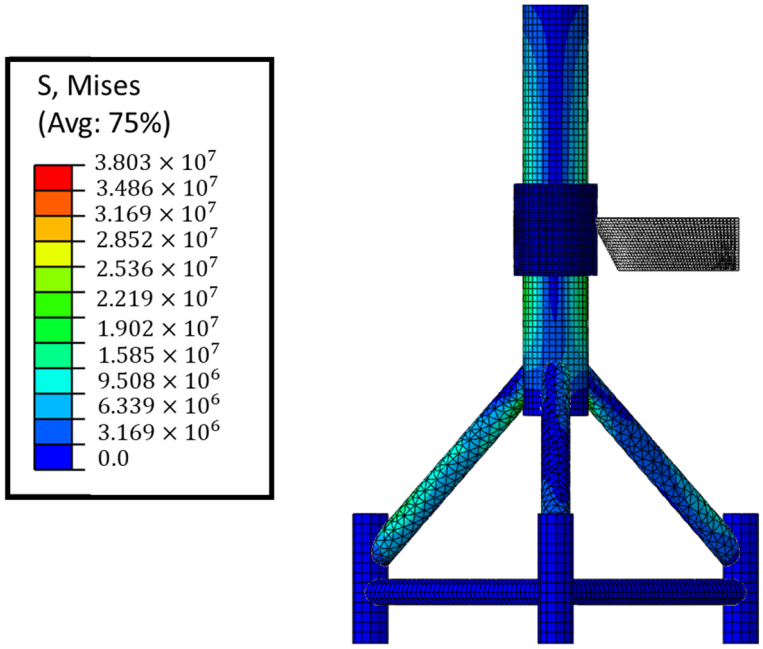


(**c**)

**Figure 14.** Mises Stress distribution of the OWT with the different materials. (**a**) AFS fender; (**b**) ACS fender; (**c**) PUFS fender.

The multi-impact response of each fender is plotted in Figure 15. The AFS fender showed a better energy absorption response, as the area under the load-displacement curves was larger than those of the ACS and PUFS fenders.

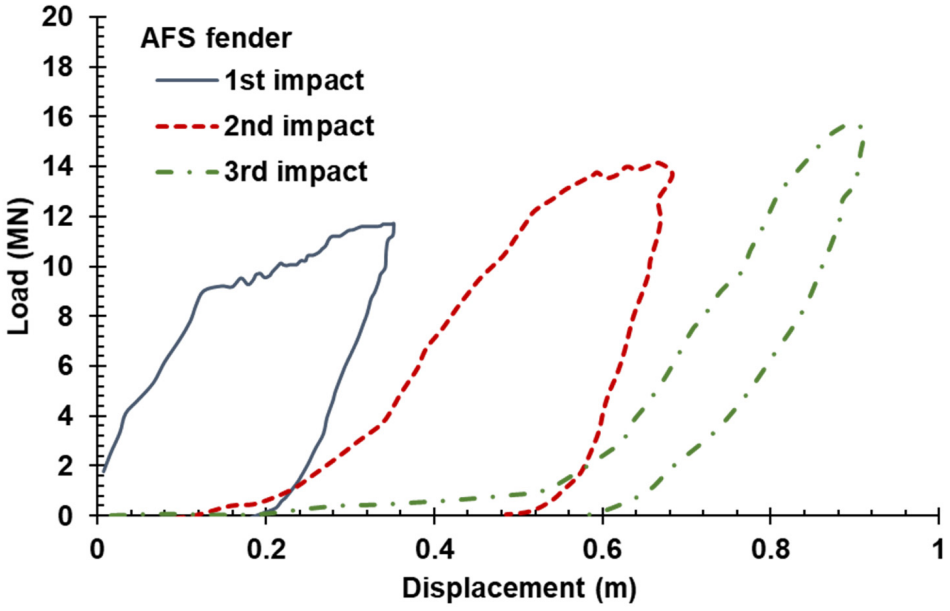


(**a**)

**Figure 15.** *Cont.*

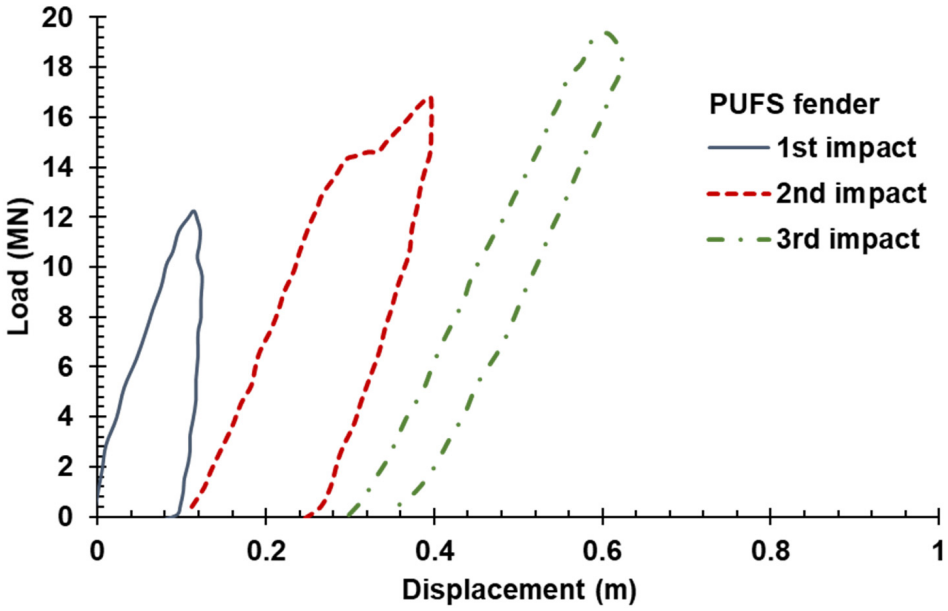


(**b**)

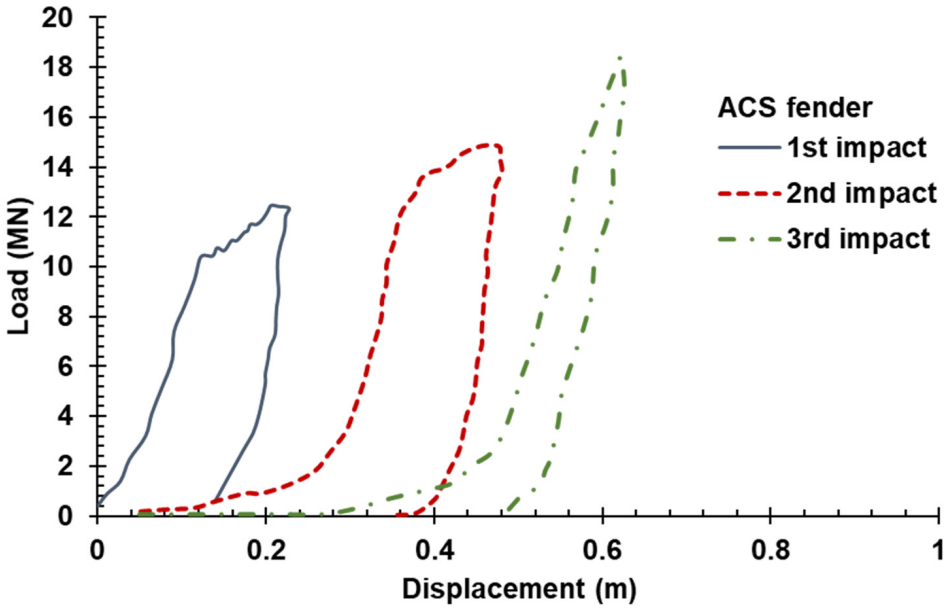


(**c**)

**Figure 15.** Multi-impact responses of the OWT-Ship impact scenario with different materials. (**a**) AFS fender; (**b**) PUFS fender; (**c**) ACS fender.

Comparing the sequence of impacts, the responses of the third impact showed a higher linearity due to the larger contribution of inner rubber layer on the fender. For the first impact, the captured reaction load for the PUFS fender was 18% and 5% larger than those of the AFS and ACS fenders, respectively. During the second impact, the contribution of fenders to energy dissipation increased by taking more damage in the crushable layer. The larger area under the load-displacement indicates that AFS fender was able to convert the impact energy to plastic dissipated and damage lost energies more effectively than the two other fenders. Interestingly, all the three fenders showed similar behavior during the third impact, i.e., the load response linearly increased and then decreased in the same fashion, which showed the full failure of the crushable layer and the contribution of the rubber layer in terms of taking and rebounding the impact energy.

The acceleration-time curves at the top of the main column are plotted in Figure 16. This parameter was analyzed at the location of the nacelle, as it is an important part of the safety of the unit operation during collisions. This part of the OWT holds the blades, whose magnitude of vibration during impact can significantly determine the OWT safety. In the case of the PUFS fender, the largest amount of vibration and the highest recorded accelerations occurred. The black box shows the area of the OWT exposed to the third impact, in which the maximum value of acceleration for the OWT with PUFS fender was 40 m/s$^2$, which was 60% and 53% greater than those of AFS and ACS fenders. The best performance among all the fenders was observed with the AFS that interestingly absorbed the kinetic energy, providing superior stability to the nacelle.

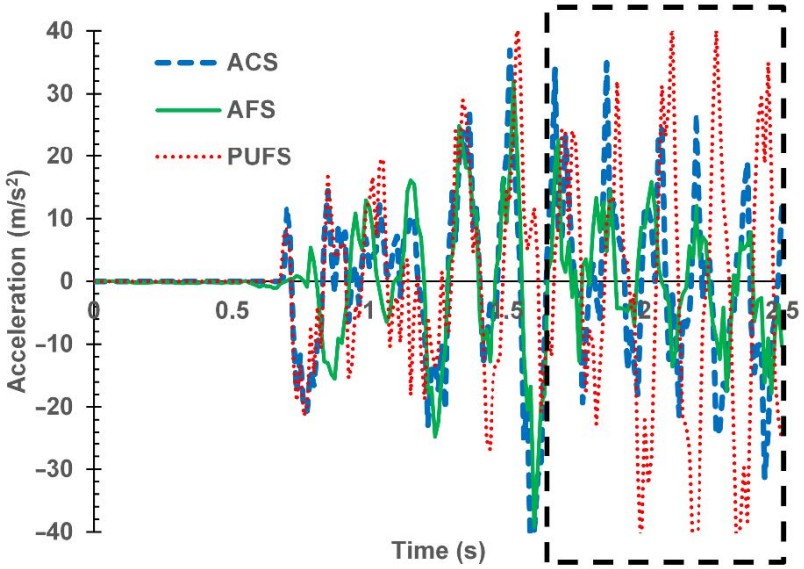


**Figure 16.** Acceleration–time curves at the nacelle of the OWT.

The kinetic energy of the model in each impact sequence is plotted in Figure 17. The PUFS fender showed the smallest reduction in the kinetic impact over the course of three impacts. The AFS and ACS fenders showed comparable behavior in terms of energy absorption; however, the rebounding energy after each impact for the AFS fender was lower than that of the ACS fender.

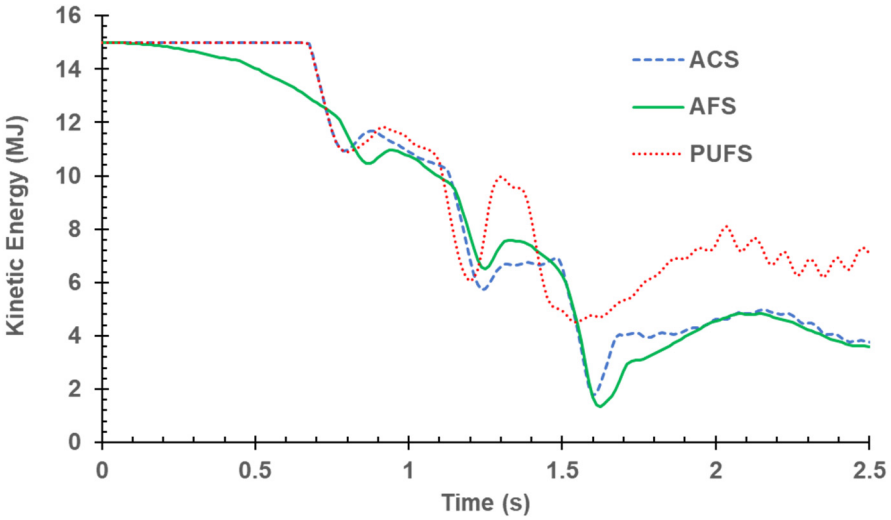


**Figure 17.** Kinetic energy-time curves.

The kinetic energy of the ACS and AFS fenders after the third impact was approximately identical, because the crushable layers in these fenders failed and the inner rubber layer played the dominant role.

## 4. Conclusions

The impact responses of three different lightweight materials (aluminum foam, agglomerate cork, and polyurethane foam) were investigated for potential application in offshore structures. Low velocity impact (LVI) tests, carried out at energy values ranging from 15 J to 35 J, demonstrated that the aluminum foam represented the best solution.

In this investigation, a Metallic Foam Shell (MFS) device made of aluminum foam sandwich (AFS) was proposed for the fender of an offshore wind turbine (OWT) and was compared with two other devices made of either agglomerate cork or polyurethane foam sandwiches. An OWT–ship collision scenario was simulated using a nonlinear finite element (FE) model. Firstly, the FE model was validated considering data taken from the literature. Then, it was developed to compare the responses of the fenders, made of investigated lightweight materials, under repeated impacts from a ship bow. The FE results demonstrated that the fender with the proposed MFS device achieved the best performance.

Many collision scenarios exist and OWT structures may be involved in collisions with ships from bow, stern, or side. The present study considered only collisions between an OWT and a ship bow to obtain a validated FE model. This research needs elaboration, i.e., investigating other collision scenarios and solving the limitations of the proposed solution.

Among the current limitations of the proposed fender, the main one is its manufacturing procedure. Sandwich type structures can be manufactured by two processes: The easiest way is ex situ, i.e., the component elements (face and core) should be cut to the desired dimensions and then glued with a special adhesive (depending on the type of used core); The second method is the in-situ one, i.e., where first the outer shell (face) of the sandwich is obtained, and then the core is obtained through different manufacturing processes, depending on its type. In the latter case, no additional glue is needed, because the core automatically adheres to the face of the sandwich during its formation process.

However, the cost difference between the two methods is significant. The in situ method requires special molds to obtain the core of the sandwich, and the foaming process together with the face of the sandwich is quite complex. The material of the sandwich face also matters here because it must withstand high temperatures during the foaming process. In addition, studies carried out on different composite structures showed that tubes filled ex situ absorb a greater amount of energy than those filled in situ. This advantage is due to the failure mechanisms that occur at the face–tube interface, as well as to the face–tube interaction effect. Therefore, the ex situ method is preferable.

The idea of the authors was to post-produce the sandwich after AFS with the ex situ procedure. The proposal is to produce curved, large AFS panels to be joined by TIG welding. Thus, according to the authors, the main limitation is that the fender must be assembled in situ. The assembly can be divided in two phases: the first (skins-core) is completed during the manufacturing process of the panels. The second occurs when the device is installed on the OWT (welding of the curved sandwich panels).

**Author Contributions:** Conceptualization, G.E. and V.C.; methodology, H.M. and V.C.; investigation, F.D., G.E. and E.L.; resources, L.G. and E.L.; data curation, H.M., F.D., G.E. and E.L.; writing—original draft preparation, H.M., G.E. and V.C.; writing—review and editing, H.M., G.E., E.L. and V.C.; visualization, H.M. and F.D.; supervision, V.C. All authors have read and agreed to the published version of the manuscript.

**Funding:** This research received no external funding.

**Institutional Review Board Statement:** Not applicable.

**Informed Consent Statement:** Not applicable.

**Data Availability Statement:** Not applicable.

**Conflicts of Interest:** The authors declare no conflict of interest.

## References


1. Palomba, G.; Epasto, G.; Crupi, V. Lightweight sandwich structures for marine applications: A review. *Mech. Adv. Mater. Struct.* **2021**, 1–26. [CrossRef]
2. Birman, V.; Kardomateas, G.A. Review of current trends in research and applications of sandwich structures. *Compos. Part B Eng.* **2018**, *142*, 221–240. [CrossRef]
3. Sharma, N.; Gibson, R.F.; Ayorinde, E.O. Fatigue of Foam and Honeycomb Core Composite Sandwich Structures: A Tutorial. *J. Sandw. Struct. Mater.* **2006**, *8*, 263–319. [CrossRef]
4. Harte, A. The fatigue strength of sandwich beams with an aluminium alloy foam core. *Int. J. Fatigue* **2001**, *23*, 499–507. [CrossRef]
5. Demelio, G.; Genovese, K.; Pappalettere, C. An experimental investigation of static and fatigue behaviour of sandwich composite panels joined by fasteners. *Compos. Part B Eng.* **2001**, *32*, 299–308. [CrossRef]
6. Epasto, G.; Distefano, F.; Mozafari, H.; Linul, E.; Crupi, V. Nondestructive evaluation of aluminium foam panels subjected to impact loading. *Appl. Sci.* **2021**, *11*, 1148. [CrossRef]
7. Hazizan, A.; Cantwell, W.J. The low velocity impact response of an aluminium honeycomb sandwich structure. *Compos. Part B* **2003**, *34*, 679–687. [CrossRef]
8. Hazizan, A.; Cantwell, W.J. The low velocity impact response of foam-based sandwich structures. *Compos. Part B* **2002**, *33*, 193–204. [CrossRef]
9. Foo, C.C.; Seah, L.K.; Chai, G.B. Low-velocity impact failure of aluminium honeycomb sandwich panels. *Compos. Struct.* **2008**, *85*, 20–28. [CrossRef]
10. Linul, E.; Marsavina, L.; Kováčik, J. Collapse mechanisms of metal foam matrix composites under static and dynamic loading conditions. *Mater. Sci. Eng. A* **2017**, *690*, 214–224. [CrossRef]
11. Sun, G.; Huo, X.; Wang, H.; Hazell, P.J.; Li, Q. On the structural parameters of honeycomb-core sandwich panels against low-velocity impact. *Compos. Part B Eng.* **2021**, *216*, 108881. [CrossRef]
12. Gilioli, A.; Sbarufatti, C.; Manes, A.; Giglio, M. Compression after impact test (CAI) on NOMEX$^{TM}$ honeycomb sandwich panels with thin aluminum skins. *Compos. Part B Eng.* **2014**, *67*, 313–325. [CrossRef]
13. Sun, M.; Wowk, D.; Mechefske, C.; Alexander, E.; Kim, I.Y. Surface and honeycomb core damage in adhesively bonded aluminum sandwich panels subjected to low-velocity impact. *Compos. Part B Eng.* **2022**, *230*, 109506. [CrossRef]
14. Baral, N.; Cartié, D.D.R.; Partridge, I.K.; Baley, C.; Davies, P. Improved impact performance of marine sandwich panels using through-thickness reinforcement: Experimental results. *Compos. Part B Eng.* **2010**, *41*, 117–123. [CrossRef]
15. Li, Y.; Wu, X.; Xiao, W.; Wang, S.; Zhu, L. Experimental study on the dynamic behaviour of aluminium honeycomb sandwich panel subjected to ice wedge impact. *Compos. Struct.* **2022**, *282*, 115092. [CrossRef]
16. Wu, X.; Li, Y.; Cai, W.; Guo, K.; Zhu, L. Dynamic responses and energy absorption of sandwich panel with aluminium honeycomb core under ice wedge impact. *Int. J. Impact Eng.* **2022**, *162*, 104137. [CrossRef]
17. Palomba, G.; Epasto, G.; Sutherland, L.; Crupi, V. Aluminium honeycomb sandwich as a design alternative for lightweight marine structures. *Ships Offshore Struct.* **2021**, 1–12. [CrossRef]
18. Palomba, G.; Scattareggia Marchese, S.; Crupi, V.; Garbatov, Y. Cost, Energy Efficiency and Carbon Footprint Analysis of Hybrid Light-Weight Bulk Carrier. *J. Mar. Sci. Eng.* **2022**, *10*, 957. [CrossRef]
19. Han, Z.; Li, C.; Deng, Y.; Liu, J. The analysis of anti-collision performance of the fender with offshore wind turbine tripod impacted by ship and the coefficient of restitution. *Ocean Eng.* **2019**, *194*, 106614. [CrossRef]
20. Zhang, Y.; Li, Y.; Guo, K.; Zhu, L. Dynamic mechanical behaviour and energy absorption of aluminium honeycomb sandwich panels under repeated impact loads. *Ocean Eng.* **2021**, *219*, 108344. [CrossRef]
21. He, X.; Soares, C.G. Experimental study on the dynamic behavior of beams under repeated impacts. *Int. J. Impact Eng.* **2021**, *147*, 103724. [CrossRef]
22. Zhu, L.; Guo, K.; Li, Y.; Yu, T.X.; Zhou, Q. Experimental study on the dynamic behaviour of aluminium foam sandwich plates under single and repeated impacts at low temperature. *Int. J. Impact Eng.* **2018**, *114*, 123–132. [CrossRef]
23. Guo, K.; Zhu, L.; Li, Y.; Yu, T.X.; Shenoi, A.; Zhou, Q. Experimental investigation on the dynamic behaviour of aluminum foam sandwich plate under repeated impacts. *Compos. Struct.* **2018**, *200*, 298–305. [CrossRef]
24. Sun, X.; Huang, D.; Wu, G. The current state of offshore wind energy technology development. *Energy* **2012**, *41*, 298–312. [CrossRef]
25. Lee, J.; Zhao, F. *GWEC Global Wind Report 2021*; Global Wind Energy Council: Brussels, Belgium, 2021.
26. Hao, E.; Liu, C. Evaluation and comparison of anti-impact performance to offshore wind turbine foundations: Monopile, tripod, and jacket. *Ocean Eng.* **2017**, *130*, 218–227. [CrossRef]
27. Liu, C.; Hao, E.; Zhang, S. Optimization and application of a crashworthy device for the monopile offshore wind turbine against ship impact. *Appl. Ocean Res.* **2015**, *51*, 129–137. [CrossRef]
28. Storheim, M.; Amdahl, J. Design of offshore structures against accidental ship collisions. *Mar. Struct.* **2014**, *37*, 135–172. [CrossRef]
29. Buldgen, L.; Le Sourne, H.; Pire, T. Extension of the super-elements method to the analysis of a jacket impacted by a ship. *Mar. Struct.* **2014**, *38*, 44–71. [CrossRef]

30. Jia, H.; Qin, S.; Wang, R.; Xue, Y.; Fu, D.; Wang, A. Ship collision impact on the structural load of an offshore wind turbine. *Glob. Energy Interconnect.* **2020**, *3*, 43–50. [CrossRef]
31. Bela, A.; Le Sourne, H.; Buldgen, L.; Rigo, P. Ship collision analysis on offshore wind turbine monopile foundations. *Mar. Struct.* **2017**, *51*, 220–241. [CrossRef]
32. Mo, R.; Li, M.; Kang, H. Transient behaviour of grouted connections of offshore wind turbines subject to ship impact. *Appl. Ocean Res.* **2018**, *76*, 159–173. [CrossRef]
33. Qiu, A.; Lin, W.; Ma, Y.; Zhao, C.; Tang, Y. Novel material and structural design for large-scale marine protective devices. *Mater. Des.* **2015**, *68*, 29–41. [CrossRef]
34. Zhu, L.; Liu, W.; Fang, H.; Chen, J.; Zhuang, Y.; Han, J. Design and simulation of innovative foam-filled Lattice Composite Bumper System for bridge protection in ship collisions. *Compos. Part B Eng.* **2019**, *157*, 24–35. [CrossRef]
35. Lin, H.; Han, C.; Yang, L.; Karampour, H.; Luan, H.; Han, P.; Xu, H.; Zhang, S. Dynamic Performance and Crashworthiness Assessment of Honeycomb Reinforced Tubular Pipe in the Jacket Platform under Ship Collision. *J. Mar. Sci. Eng.* **2022**, *10*, 1194. [CrossRef]
36. Epasto, G.; Distefano, F.; Gu, L.; Mozafari, H.; Linul, E. Design and optimization of Metallic Foam Shell protective device against flying ballast impact damage in railway axles. *Mater. Des.* **2020**, *196*, 109120. [CrossRef]
37. Duarte, I.; Vesenjak, M.; Krstulović-Opara, L. Dynamic and quasi-static bending behaviour of thin-walled aluminium tubes filled with aluminium foam. *Compos. Struct.* **2014**, *109*, 48–56. [CrossRef]
38. Miller, W.; Zhuang, L.; Bottema, J.; Wittebrood, A.; De Smet, P.; Haszler, A.; Vieregge, A. Recent development in aluminium alloys for the automotive industry. *Mater. Sci. Eng. A* **2000**, *280*, 37–49. [CrossRef]
39. Simancik, F.; Rajner, W.; Laag, R. *Alulight—Aluminum Foam for Lightweight Construction*; SAE International: Warrendale, PA, USA, 2000.
40. Banhart, J.; García-Moreno, F.; Heim, K.; Seeliger, H.W. Light-Weighting in Transportation and Defence Using Aluminium Foam Sandwich Structures. In *Light Weighting for Defense, Aerospace, and Transportation*; Indian Institute of Metals Series; Gokhale, A.A., Prasad, N., Basu, B., Eds.; Springer: Singapore, 2019; pp. 61–72.
41. Moulas, D.; Shafiee, M.; Mehmanparast, A. Damage analysis of ship collisions with offshore wind turbine foundations. *Ocean Eng.* **2017**, *143*, 149–162. [CrossRef]
42. *ISO 13314*; Mechanical Testing of Metals—Ductility testing—Compression Test for Porous and Cellular Metals. ISO: Geneva, Switzerland, 2011.
43. *ISO 844*; Rigid Cellular Plastics—Determination of Compression Properties. ISO: Geneva, Switzerland, 2011.
44. *ASTM D 1621*; Standard test method for compressive properties of rigid cellular plastics. ASTM: West Conshohocken, PA, USA, 2000.
45. He, X.; Rong, J.; Xiang, D. Damage Analysis of Aluminium Foam Panel Subjected to Underwater Shock Loading. *Shock Vib.* **2017**, *2017*, 6031414. [CrossRef]
46. Hooputra, H.; Gese, H.; Dell, H.; Werner, H. A comprehensive failure model for crashworthiness simulation of aluminium extrusions. *Int. J. Crashworthiness* **2004**, *9*, 449–464. [CrossRef]
47. Roven, H.J.; Nesboe, H.; Werenskiold, J.C.; Seibert, T. Mechanical properties of aluminium alloys processed by SPD: Comparison of different alloy systems and possible product areas. *Mater. Sci. Eng. A* **2005**, *410–411*, 426–429. [CrossRef]